

# Mesospheric vertical thermal structure and winds on Venus from HHSMT CO spectral-line Observations

Miriam Rengel<sup>\*</sup>, Paul Hartogh, Christopher Jarchow

*Max-Planck-Institut für Sonnensystemforschung, Max-Planck-Strasse 2,  
37191, Katlenburg-Lindau, Germany*

---

## Abstract

We report vertical thermal structure and wind velocities in the Venusian mesosphere retrieved from carbon monoxide ( $^{12}\text{CO}$  J = 2-1 and  $^{13}\text{CO}$  J = 2-1) spectral line observations obtained with the Heinrich Hertz Submillimeter Telescope (HHSMT). We observed the mesosphere of Venus from two days after the second Messenger flyby of Venus (on June 5 2007 at 23:10 UTC) during five days. Day-to-day and day-to-night temperature variations and short-term fluctuations of the mesospheric zonal flow were evident in our data. The extensive layer of warm air detected recently by SPICAV at 90 – to 100 km altitude is also detected in the temperature profiles reported here.

These data were part of a coordinated ground-based Venus observational campaign in support of the ESA Venus Express mission. Furthermore, this study attempts to cross-calibrate space and ground-based observations, to constrain radiative transfer and retrieval algorithms for planetary atmospheres, and to contribute to a more thorough understanding of the global patterns of circulation of the Venusian atmosphere.

## 1 Introduction

2 Understanding the Venusian atmospheric dynamics is one of the fundamental  
3 problems in planetary sciences. Its study is of great value not only to learn  
4 about Venus itself, but also to interpret observations of extrasolar terrestrial  
5 planets, and among other examples, to understand their range of habitability.  
6 Two international missions recently joined efforts and carried out multi-point  
7 observations of the Venusian atmosphere on 6 June for several hours: NASA's  
8 MESSENGER spacecraft swung by Venus for a second time on 5 June 2007 at  
9 23:10 UTC on its way to Mercury, and ESA's Venus Express is orbiting around  
10 Venus since 11 April 2006. Among the space-based observations, a world-wide  
11 coordinated Earth-based Venus observational campaign from 23 May 2007  
12 to June 9 (and later) was initiated to remotely observe the Venusian atmo-  
13 sphere<sup>1</sup>. Because Venus was close to its maximum eastern elongation during  
14 June 2007, Venus was in a favourable position for ground-based observations  
15 of both its day- and nightside.

16 The Venusian atmosphere is conventionally divided into three regions: the  
17 troposphere (below 70 km), the mesosphere (70 - 120 km), and the ther-  
18 mosphere (above 120 km). Studying the Venus' mesosphere dynamics is of  
19 special interest because this transition region is characterized by the combi-

---

\* Corresponding author.

*Email address:* [rengel@mps.mpg.de](mailto:rengel@mps.mpg.de) (Miriam Rengel).

*URL:* <http://www.mps.mpg.de/homes/rengel/> (Miriam Rengel).

<sup>1</sup> <http://sci.esa.int/science-e/www/object/index.cfm?fobjectid=41012>

20 nation of two different wind regimes (a retrograde super-rotation of the lower  
21 atmosphere, and a sub-solar to anti-solar flow pattern, SS-AS, of the upper  
22 atmosphere), and affects both the chemical stability and the thermal structure  
23 of the entire atmosphere (Clancy et al., 2003). The principal feature of Venus’  
24 atmospheric general circulation is the zonal super-rotation with typical wind  
25 velocities of 60–120 m s<sup>-1</sup> at the cloud top and nearly zero on the ground. An  
26 important (best measured) tracer of the atmospheric motion of Venus is car-  
27 bon monoxide (CO) (Kakar et al., 1976; Wilson et al., 1981). Sub-millimetre  
28 spectral line observations of CO and its isotopes play an important role in  
29 the investigation of the poorly constrained Venus mesosphere (it is the only  
30 technique to provide direct wind measurements in the mesosphere): they are  
31 used to retrieve vertical profiles of CO, temperature, and winds at the meso-  
32 spheric altitudes (e.g., Clancy and Muhleman (1991); Lellouch et al. (1994);  
33 Clancy et al. (2003); Rengel et al. (2008)).

34 Data capabilities and partial preliminary results from the submillimetre ob-  
35 servations of the CO lines carried out with the Heinrich Hertz Submillimeter  
36 Telescope (HHSMT) during June 2007 on the mesosphere of Venus as a part  
37 of the ground-based observing campaign were reported in Rengel et al. (2008).

38 In this paper, we present a complete retrieval analysis of the data obtained,  
39 and report of mesospheric parameters such as wind, vertical thermal structure,  
40 and CO abundance derived from the <sup>12</sup>CO J = 2–1 and <sup>13</sup>CO J = 2–1 lines  
41 by the use of a radiative transfer model and retrieval algorithm. Section 2  
42 summarizes the observations and describes the data reduction. The results are  
43 presented in Section 3. Spacial/temporal changes in the mesospheric thermal  
44 structure and winds are discussed in Section 4.

## 45 2 Observations and data reduction

46 CO observations on the disk of Venus were carried out at the HHSMT, oper-  
47 ated and owned by the Arizona Radio Observatory (ARO). The telescope is  
48 located at an elevation of 3178 m on Mount Graham, Arizona, and consists of  
49 a 10-m diameter primary with a nutating secondary. Our 8, 9, 10, 14 and 15  
50 June from 18:30 to 0:30 UT observations employed the 345 Superconductor-  
51 Insulator Superconductor (SIS) and the 2mmJT/1.3mmJT ALMA Sideband  
52 Separating<sup>2</sup> receivers, operating respectively at 320–375 and 210–279 GHz  
53 to observe the <sup>12</sup>CO J = 2-1 (at a frequency of 230.54 GHz), <sup>12</sup>CO J = 3-2  
54 (at 345.79 GHz), and <sup>13</sup>CO J = 2-1 (at 220.398 GHz) rotational transitions.  
55 The 345 SIS double sideband receiver was used with the signal frequency be-  
56 ing placed once in the lower sideband (LSB) and another time in the upper  
57 sideband (USB), and the 2mmJT/1.3mmJT one only in LSB. We used si-  
58 multaneously seven different backends: two 1 MHz Forbes filterbanks (FFBA  
59 and FFBB), two 970 MHz wide Acousto-Optical-Spectrometers (AOSA and  
60 AOSB, with mean resolutions of 934 kHz for AOSA and 913 kHz for AOSB),  
61 two FB2 (FB2A and FB2B) filterbackends, and one 215 MHz CHIRP Trans-  
62 form spectrometer (CTS, resolution of ~40 kHz) (Hartogh and Hartmann,  
63 1990; Villanueva and Hartogh, 2006).

64 Observing conditions were generally good, although on 10, 14 and 15 June it

---

<sup>2</sup> developed as part of the ALMA project, this system is the first of this kind to incorporate the latest SIS mixer technology: image-separating mixers. Here, the image separating system operates truly separating image noise and signal. It uses an old 1.3mm and 2mm quasioptical JT Dewar and cross-grid to separate the two orthogonal linear polarizations.

65 was partially cloudy. System temperatures were typically 1500-2500 for the 345  
66 GHz receiver and 200-500 K for the 2mmJT/1.3mmJT receiver. The observing  
67 mode was always dual beam switching. Pointing was checked every 2–3 h. The  
68 typical integration time per individual spectrum was around 4 min.

69 The Venus disc had a diameter of 23.44'' at the beginning and 25.55'' at the  
70 end of our observational period, with the evening terminator separating the  
71 dayside crescent (the fraction of illumination for Venus was 49.95 and 45.68%,  
72 as seen by observer). Fig. 1 in Rengel et al. (2008) shows a synthetic image of  
73 the apparent disc of Venus that approximates the telescopic view of Venus as  
74 seen from the Earth at 8 June and 18:30 UT.

75 An overview of the complete data set can be found in Rengel et al. (2008).  
76 We obtained measurements for  $^{12}\text{CO}$   $J = 2-1$  at seven positions (including  
77 centre, east and west limbs on the Venus disc) and for  $^{13}\text{CO}$   $J = 2-1$  at one  
78 (centre), see Fig. 1. The retrieval of the temperature profile and winds requires  
79 a clean spectrum (spectrum with minor or almost zero baseline features), and  
80 the CTS with a high dynamical range larger than 30 dB is well suited for our  
81 goals, here we concentrate only on the data taken with the CTS. The  $^{12}\text{CO}$   $J$   
82  $= 3-2$  line observations were substantially noisier than  $^{12}\text{CO}$   $J = 2-1$ , so they  
83 are not considered in our analysis here. Table 1 gives a summary of our  $^{12}\text{CO}$   
84  $J = 2-1$  and  $^{13}\text{CO}$   $J = 2-1$  observations.

85 The initial reduction of each spectrum was performed using the CLASS soft-  
86 ware package of the Grenoble Astrophysics Group<sup>3</sup>.

---

<sup>3</sup> <http://www.iram.fr/IRAMFR/GILDAS>

### 87 **3 Data analysis: retrieval of mesospheric parameters (vertical ther-** 88 **mal structure, CO abundance, and winds)**

#### 89 *3.1 Vertical thermal structure and CO profile*

90 In order to retrieve the temperature profile in the mesosphere, we have ap-  
91 plied a retrieval technique described by C. D. Rodgers as optimal estimation  
92 (Rodgers, 1976). We used a radiative transfer code (Jarchow and Hartogh,  
93 1995; Jarchow, 1998; Hartogh and Jarchow, 2004) which describes the physics  
94 of the radiative transfer through the atmosphere, i.e., describes the transport  
95 and balance of energy within the atmosphere, to calculate the synthetic spec-  
96 tra which best fit the observed spectra. An a priori profile is required as initial  
97 input for the optimal estimation technique. A priori atmospheric temperature  
98 profiles, for day and nightsides, were taken from the Venus international ref-  
99 erence atmosphere (VIRA) (Kliore et al., 1992). For observations centred on  
100 the evening terminator, a uniform profile at 172 K at altitudes higher than  
101 90 km was considered as approximation (and the VIRA profile at altitudes  
102 lower than 90 km). The a priori CO vertical profile employed is described in  
103 the paragraph below. For the analysis here these profiles were automatically  
104 included in the points distributed throughout the disc (Fig. 2). Fig. 2 shows  
105 how we calculated the disc-averaged spectrum. For each black dot a pencil  
106 beam spectrum (convolved with the telescope 2D Gaussian beam pattern) has  
107 been calculated. The rings show the grouping of the dots. Within a ring each  
108 dot has the same distance from the centre of the planetary disc. The density  
109 of the dots has been chosen according to the variation of the spectra: low  
110 density at the disc centre and high density at the limb, because the spectra

111 of the single pencil beams vary only slowly at the centre, while due to the  
112 exponential density decrease of the atmosphere with altitude the limb area  
113 has to be resolved much higher. We sub-divided the limb area into 16 rings  
114 to model accurately the contribution of the limb region to the disc-averaged  
115 spectra.

116 Our atmospheric model consisted of 46 layers spanning the 30-120 km interval  
117 with a resolution of 2 km. Upwelling continuum emission from the  $\sim 55$  km  
118 altitude region is modelled by incorporating the collision induced absorption  
119 of  $\text{CO}_2$  (Gruszka and Borysow, 1997) and using the VIRA temperature data at  
120 this altitude. Initially, the observed spectra were modelled in units of percent  
121 absorption and then converted to absolute brightness temperature by rescaling  
122 the spectra in such a way that the continuum brightness temperature equal  
123 to the VIRA temperature around 55 km.

124 We derived the CO mixing ratio profile from the simultaneous fitting of  $^{12}\text{CO}$   
125  $J = 2-1$  and  $^{13}\text{CO } J = 2-1$  HHSMT spectra (Fig. 10, Obs. 35 and 36). Both  
126 observations constrain CO abundances over different ranges of altitude since  
127 they have a different opacity. Two lines of the same molecule with strongly  
128 different altitude dependent opacity allow retrieving simultaneously the ver-  
129 tical profiles of temperature and its volume mixing ratio. Unfortunately we  
130 have only two cases in which we observed two lines at the same time. Obs. 35,  
131 pointing only at the disc centre was the least noisy one. We decided to re-  
132 trieve the vertical profile of CO from this observation and use it as a priori  
133 profile for all other retrievals presented in this paper. We stress that simul-  
134 taneous temperature/CO retrievals are less reliable when only  $^{12}\text{CO } J = 2-1$   
135 data are available. The mentioned solely joint retrieval employed as a priori  
136 a CO mixing ratio profile purely increasing exponentially with the altitude,

137 a profile similar to the average of the profiles of Figure 8 A-B in Clancy and  
138 Muhleman (1991). Note that we did not fix the CO profile with zero error in  
139 the temperature from a single CO spectra line observation but left error bars  
140 unequal zero on it, i.e., the error bars we got from the CO retrieval. The reason  
141 not to fix the CO profile in the retrieval (error bars zero) is that in reality the  
142 CO profile is variable and each measurement, even with highest accuracy is  
143 just a snapshot for the moment of the observation. In other words, for a single  
144  $^{12}\text{CO}$  line observation we give the fit algorithm the freedom to not only fit the  
145 temperature profile, but to a small extend also the CO profile. However, while  
146 for the CO profile retrieval with two lines the correlation length for the CO  
147 profile was only 10 km (providing almost the same vertical resolution) in the  
148 case of a single line retrieval the correlation length has been set to 40 km. In  
149 other words, the fit algorithm can hardly modify the (exponential) shape of  
150 the CO-profile, but almost just shift it forth and back as a whole within the  
151 (relatively small) error bars.

152 The capability of the fitting algorithm to retrieve the atmospheric tempera-  
153 ture, CO-profile, and winds can be characterized by the so-called weighting  
154 functions  $K_x$  as defined by Rodgers 1990. Here we briefly present the proce-  
155 dure we followed in order to calculate  $K_x$ . Representing the atmosphere by a  
156 set of  $N$  layers allows to write the atmospheric profiles as a state vector  $x$ ,  
157 where  $x$  is a vector of unknowns to be retrieved from the measurements  $y$ .  $y$  is  
158 a vector of measured quantities (i.e., the CO spectrum measured at  $m$  discrete  
159 frequencies). The so-called forward model  $F(x)$  relates  $x$  to  $y$  as  $y = F(x)$ .  
160 This forward model contains the complete physics necessary to calculate the  
161 absorption coefficient as a function of temperature, mixing ratio, and spectral  
162 line parameters, and in addition performs the radiation transfer through the

163 atmosphere. It is in general a non-linear function of the vector  $x$  of unknowns.

164 The weighting functions  $K_x$  are now defined as  $K_x = \partial F(x) / \partial x$ . They describe  
165 the sensitivity of the measurement, which means the observed CO spectrum,  
166 with respect to each single parameter to be retrieved. Using  $K_x$  allows to  
167 linearize the forward model around a reference state  $\bar{x}$ :

$$168 \quad y = F(\bar{x}) + \frac{\partial F(\bar{x})}{\partial x} \cdot (x - \bar{x}). \quad (1)$$

169 For the calculation of  $K_x$  here we used as reference state the a priori pro-  
170 files and normalized the resulting curves to unity as maximum value. Because  
171 the measurement depends in a different way on atmospheric temperature and  
172 CO mixing ratio, the weighting functions have to be different for the temper-  
173 ature and mixing ratio. As seen later, this is most strikingly visible at the  
174 altitude around 55 km: here the collision induced absorption of CO<sub>2</sub> in Venus  
175 atmosphere creates a sensitivity of the spectrum with respect to tempera-  
176 ture, independent of the CO mixing ratio. On the other hand, the spectrum  
177 is not sensitive to the CO mixing ratio around this altitude anymore, because  
178 the same CO<sub>2</sub> absorption lets the atmosphere become optically thick below  
179 55 km. Finally, if the weighting functions are zero in a certain altitude range  
180 this means here the observation does not depend on the atmospheric param-  
181 eters, and consequently there parameters cannot be retrieved at this altitude  
182 range.

183 Introducing the inverse model  $I$ , which relates the retrieved atmospheric state  
184  $\hat{x}$  to  $y$ ,  $\hat{x} = I(y)$ , and combining it with the forward model  $y = F(x)$ , allows  
185 to define a transfer function  $T$ :

$$186 \quad \hat{x} = I(F(x)) = T(x). \quad (2)$$

187 The averaging kernels  $A$  are now defined as  $A = \partial T(x)/\partial x$  and describe the  
188 sensitivity of the retrieved atmospheric parameters with respect to each single  
189 true parameter. For each parameter, for example, a temperature at a certain  
190 altitude, there is an averaging kernel function, showing that this temperature  
191 depends on a change of the true temperature at all other altitudes.

192 Normalized temperature and CO-weighting functions for  $^{12}\text{CO}$   $J = 2-1$  (with  
193 separate panels for the nightside and dayside) and  $^{13}\text{CO}$   $J = 2-1$  for several  
194 frequency offsets around each transition are presented in Figs. 3–4, and in  
195 Fig. 5, respectively. They show the vertical range and resolution of temperature  
196 and of CO retrievals afforded here: temperature sensitivity for  $^{12}\text{CO}$   $J = 2-1$   
197 is primarily confined to the 55–110 km range,  $^{12}\text{CO}$   $J = 2-1$  sensitivity to 68–  
198 90 km range, temperature sensitivity for  $^{13}\text{CO}$   $J = 2-1$  to 55–100 km range,  
199 and  $^{13}\text{CO}$   $J = 2-1$  sensitivity to 70–95 km range. Because of the input CO  
200 profile, the vertical distribution of the CO weighting functions in Fig. 4 are  
201 not greatly influenced by day-to-night variation of CO abundances. However,  
202 the divergence of day and night temperature profiles creates significant offsets  
203 in day and night altitude scales above 90 km altitude.

204 In Figs. 6–11 we present the measured and fitted spectra, and retrieved tem-  
205 perature profiles and CO distribution for the observations in Table 1 obtained  
206 with our technique (Figs. 6–10 and Fig. 11 (upper panels) for  $^{12}\text{CO}$   $J = 2-1$   
207 and Fig. 11 (lower panels) for  $^{13}\text{CO}$   $J = 2-1$  lines). Lower panels from the  
208 spectra boxes in Figs. 6–11 show difference between the observed and fitted  
209 spectra, and averaging kernels for temperature, CO, and winds, respectively.  
210 Note that the differences between the measured and fitted spectra are so small  
211 that they are hardly distinguished when they are plotted simultaneously.  
212 For clarity we show only each second averaging kernel curve. Wind retrieval

213 will be addressed in the next section. Error bars represent the total error in  
214 the retrieval which comprises the contributions of measurement errors, model  
215 errors, and null-space errors due to the inherent finite vertical resolution, as  
216 described in Rodgers (1990). These error terms appear as covariance matrices  
217 (interpreted in terms of error patterns) and are equivalent to error bars. The  
218 contribution of a priori to the retrieval is described in terms of the eigenvectors  
219 of the averaging kernel matrix. For the error bar calculations we followed the  
220 recipe given in Rodgers (1990). A discussion of the correlated errors can be  
221 found in Sect. 3.3.

222 The 15 June 2007 temperature profile from Obs. 36, for example, is compared  
223 with the ones obtained from SPICAV onboard Venus Express (Bertaux et al.,  
224 2007), Pioneer Venus (PV) descent probes (Seiff et al., 1980), to the OIR  
225 sounding measurements (Schofield and Taylor, 1983), and to the PV night  
226 probe (Seiff and Kirk, 1982) (Fig. 12). We detected a temperature excess at  
227 90– to 100 km altitude which coincides with the extensive layer of warm air at  
228 altitudes 90–120 km detected by SPICAV (Bertaux et al., 2007). However, its  
229 peak shows a smaller temperature excess than the one detected by SPICAV.  
230 This particular layer has been interpreted as the result of adiabatic heating  
231 during air subsidence. Because adiabatic heating is a localized phenomenon,  
232 does the layer’s altitude increase with the latitude? We note that layers alti-  
233 tudes of around 95, 97 and 100 km are determined at latitudes of 4° S, 0°, and  
234 39° N, respectively (Bertaux et al. (2007); this work). We stress this possibil-  
235 ity, however, three-point statistics cannot make a strong statement, additional  
236 data at different latitudes are required. Furthermore, in other altitudes the  
237 HHSMT profile compares favourably to those returned by the previous mea-  
238 surements. Similar temperature profiles were also observed (Lellouch et al.,

239 1994; Clancy et al., 2003). Moreover, it was suggested that a 10–15 K increase  
240 in the mesospheric temperatures occur over 1–30–day periods, and large vari-  
241 ations (20–40 K) over as yet undetermined timescales (Clancy et al., 2003).  
242 More data over longer periods are necessary.

### 243 3.2 *Wind velocity retrieval*

244 Fig. 13 shows the observed and fitted spectrum of  $^{12}\text{CO}$   $J = 2-1$  (Obs. 27),  
245 the residual (difference between observation and fit), and the retrieved verti-  
246 cal temperature and CO profiles and respective kernels. The double peak in  
247 the centre of the residuum (left lower panel) shows that the fit between the  
248 observed and synthetic spectra has deviations, meaning that some physical  
249 parameters are still being missing in the model. Obviously, this double peak is  
250 related to a frequency shift of the fitted line relative to the observed one. This  
251 frequency shift is caused by movements of the observed air mass along the line  
252 of sight. In other words, we see the effect of winds causing Doppler shifts in  
253 the centre of the observed spectrum. In order to get a perfect fit an additional  
254 fit parameter has to be introduced, which minimizes the residual by frequency  
255 shifting the spectrometer channels around the line centre related to the wind  
256 speed as function of altitude. In more detail, we retrieved the beam-integrated  
257 wind velocities taking into account vertical information. The model assumes  
258 an individual uniform zonal wind speed within each atmospheric layer, and  
259 the layers together rotate with individual angular velocities among a common  
260 axis, the rotational axis of Venus. According to the component of the wind  
261 velocity vector along the line of sight, each location on the Venus’ disc has  
262 its own Doppler shift: it is maximum at the limb on the equator, and zero

263 for all points of the Venus' disc falling onto the rotational axis. Because the  
264 size of the main beam here is comparable to the diameter of the Venus' disc  
265 for our observational period, we integrated across the Venus' disc (see Fig. 2  
266 and explanation in the last chapter) to take into account the smoothly vary-  
267 ing Doppler shifts. Pointing exactly to the centre of the disc just causes the  
268 spectral line slightly to broaden, because the contributions from the western  
269 and eastern limb are Doppler-shifted with respect to the line centre, but in  
270 opposite directions. However, pointing to the eastern with respect to western  
271 limb causes the contribution from this limb to dominate over the contribution  
272 from the opposite limb (larger weight due to the antenna pattern) and the  
273 resulting spectral line appears to be completely red, respectively. blue shifted.  
274 This shift with respect to the nominal line centre is sufficient to retrieve a  
275 wind velocity within each individual atmospheric shell. As a priori profile we  
276 have chosen a wind speed of  $0 \text{ m s}^{-1}$  throughout the whole atmosphere, with a  
277 standard deviation of  $100 \text{ m s}^{-1}$ . The information gained by the observations  
278 will reduce the error bars in the altitude range the observations are sensitive  
279 to. Both, the upper and the lower boundary are related to spectral noise. If  
280 it exceeds a certain value, the retrieval algorithm cannot relate Doppler shifts  
281 to wind speeds smaller than  $100 \text{ m s}^{-1}$ . Concerning the wind profile vertical  
282 resolution we have assumed a correlation between the layers characterized by  
283 a correlation length of 4 km (Rodgers 1990). This value is similar to the one  
284 assumed for the temperature profile resolution (for the CO mixing ratio we  
285 assumed higher values than these ones in order to restrict the degrees of free-  
286 dom of the fitting). Wind-weighting functions for  $^{12}\text{CO}$   $J = 2-1$  line (day- and  
287 nightsides) are presented in Fig. 14, respectively. Wind sensitivity is primar-  
288 ily confined to the 85-110 km range. The altitude resolution indicated by the  
289 averaging kernels is consistent with the one indicated by the weighting func-

290 tions. Both, the weighting functions and the averaging kernels show a clear  
291 day/night dependence of the altitude in which the winds are detected. Vice  
292 versa, from the averaging kernels day and night observations can easily be  
293 identified. Fig. 6 shows wind retrievals for the Obs. 19, 20 and 21. Obs. 19 is  
294 pointing on the disc centre. The retrieved wind speed is zero as expected. Obs.  
295 20 is pointing on the night side and provides a wind speed of nearly  $300 \text{ m s}^{-1}$   
296 at 110 km altitude. The non-zero residual can be interpreted in a way, that  
297 for this observation the dayside emission is very weak and cannot compensate  
298 the emission from the nightside, therefore one-half of the double peak cannot  
299 be fitted. The wind of Obs. 22 is comparable with that of Obs. 20.

300 All the wind measurements given here are deprojected ones. Figs. 6–11 present  
301 all retrieved wind velocities, from two observing days (14 and 15 June), and  
302 Fig. 15 retrieved evident wind measurements as a function of beam position. In  
303 Fig 15, when several observations were carried out at the same beam position  
304 and day (Obs. 20, 22 and 24 at beam position 9, Obs 21 and 29 for beam  
305 position 10, and Obs. 25 and 27 for beam position 11), an averaged wind  
306 velocity is calculated (we assume that the beam is positioned at the same  
307 right ascension for the positions 9 and 14, and also for 10 and 15). Strong  
308 winds are also reported by Lellouch et al. 2008 (this issue).

### 309 *3.3 Characterization of the correlated errors*

310 The optimal estimation method as described by Rodgers 1976 does not only  
311 allow to retrieve a temperature, mixing ratio, and wind profiles from the ob-  
312 served spectra of Venus, but in addition automatically provides an error es-  
313 timate for the derived quantities. If each of the three profiles is represented

314 by a set of  $n$  discrete numbers corresponding to  $n$  discrete layers representing  
 315 the atmosphere of Venus, then the error estimation is given in the form of a  
 316 covariance matrix  $S$  with the dimension  $3n \times 3n$ . Its diagonal elements are the  
 317 variances of the profile values in each single layer and the square root of these  
 318 variances is shown in Figs. 6–11 as error bars for the retrieved profiles. How-  
 319 ever, if the off-diagonal elements of  $S$  are not zero, they indicate a correlation  
 320 of these errors, for example, the temperature profile in a certain layer with the  
 321 temperature errors within all the layers. In addition, the off-diagonal elements  
 322 also specify the correlation between the temperature, mixing ratio and wind  
 323 profile errors. In order to characterize these correlated errors we followed the  
 324 formal procedure described in Rodgers 1990 and performed as an example an  
 325 eigenvector  $\lambda$  and eigenvalue  $l$  analysis of  $S$  for the Obs. 34. This analysis pro-  
 326 vides the so-called error patterns (orthogonal quantities  $e_i = \lambda_i^{1/2} l_i$ ) which show  
 327 the correlation of the errors for all retrieved quantities. There are in total  $3n$   
 328 error patterns and each single pattern consists of a part of  $n$  numbers belonging  
 329 to the temperature,  $n$  numbers to the mixing ratio, and  $n$  numbers to wind  
 330 profiles. Because these three blocks have different physical units for plotting  
 331 purpose, a single pattern has been split and plotted into three separate panels  
 332 (left, centre and right) in Figs. 16–17. Looking through all the error patterns  
 333 suggests to sort them into three different groups: error patterns with large  
 334 amplitudes for only (1) the temperature part, (2) the mixing ratio part, and  
 335 (3) wind profile part. These three groups are shown in Fig. 16, upper, middle  
 336 and lower panels. The fact that such a separation is possible shows that the  
 337 errors of the three profiles are basically not correlated. The oscillating nature  
 338 of part of the error patterns for the wind profile, for example, indicates the  
 339 strong correlation between the wind profile errors in different layers. Looking  
 340 at the error patterns with large amplitudes for the temperature reveals (1) the

341 amplitudes are only large for altitudes outside the 70–100 km altitude range,  
342 showing that the CO spectral line contains enough information to significantly  
343 reduce the a priori profile error at this altitude; (2) there exists one error pat-  
344 tern which behaves exactly the opposite (see Fig. 16): it has a large amplitude  
345 within the 70–100 km range, but a small one outside. At the same time there  
346 is also a large error pattern amplitude for the CO profile part, which means  
347 that only in this case there is a strong correlation between the two errors. This  
348 single error pattern describes most of the error of the temperature profile in  
349 that altitude region, in which the observation is sensitive to atmospheric tem-  
350 perature. A further discussion of error patterns due to instrumental noise and  
351 null-space, and the effect of a priori data can be also based in the procedure  
352 described in Rodgers 1990, but this is beyond the scope of this paper.

## 353 4 Discussion

### 354 4.1 *Short-term changes in the mesospheric thermal structure and in winds*

355 We compare the day and night mesospheric temperature profiles from the 14  
356 and 15 June observing period in Fig. 18. Direct detailed shape comparison  
357 indicates day-to-night and day-to-day small variations. For example, largest  
358 day-to-night variations of around 25 K occur at 102 km, day-to-day variations  
359 of around 15 K occur also at 85 km, and night-to-night variations of around  
360 15 K occur also at 102 km. It must be stressed however that any variation  
361 (spatial or temporal ones) is not differentiated here. Furthermore, measure-  
362 ments acquired at longer observing periods over the Venus’ disc would define  
363 a pattern of variation (if any).

364 From Figs. 6–11, a qualitative comparison of the wind measurements suggests  
365 a day-to-day variability of the winds. For instance, for beam position 9, the  
366 velocity increases from around  $280 \text{ m s}^{-1}$  to around  $355 \text{ m s}^{-1}$  from 14 to  
367 15 June, and for beam position 10, from  $-68$  to  $-280 \text{ m s}^{-1}$  from 14 to 15  
368 June. From West-to-East limb wind comparisons (at beam positions 10 and  
369 13), we detect negative weaker winds of  $-68 \pm 89 \text{ m s}^{-1}$  and of  $-136 \pm 86 \text{ m s}^{-1}$ ,  
370 respectively. Furthermore, at beam positions 9 and 11, we detect positive winds  
371 of  $280 \pm 66 \text{ m s}^{-1}$  and of  $205 \pm 76 \text{ m s}^{-1}$ , respectively. Wind measurements in  
372 Fig. 15 are taken at the wind peak of Figs. 6–11.

## 373 5 Conclusion

374 We have carried out several HHSMT  $^{12}\text{CO J} = 2-1$  and  $^{13}\text{CO J} = 2-1$  line  
375 observations on different beam positions on Venus disc during June 2007  
376 around the MESSENGER flyby of Venus and observations from Venus Ex-  
377 press mission. From the spectra we retrieved vertical profiles of temperature,  
378 CO distribution, and wind velocities for the 2007 June mesosphere of Venus.  
379 Changes in the thermal structure of the Venus mesosphere are detected: day-  
380 to-night small temperature variations and short-term (day-to-day) on a time  
381 scale as short as one day. This is consistent with the picture of dramatic vari-  
382 ability of the Venus mesosphere with changes in temperature occurring on  
383 short scales (Clancy et al. (2005); Sandor and Clancy (2005)). Furthermore,  
384 retrieved winds show variations of around  $100 \text{ m s}^{-1}$  between the winds on 14  
385 June and those on 15 June.

386 HHSMT line observations of  $^{12}\text{CO J} = 2-1$  and  $^{13}\text{CO J} = 2-1$  and retrieved  
387 thermal profiles of the mesosphere of Venus (the temperature peak detection

388 at 90-100 km) seems to support the new finding of the extensive layer of warm  
389 air detected by SPICAV onboard Venus Express.

390 Despite the success of the analysis presented here, some points need further  
391 work. Wind measurements and fluctuations of the zonal flow will be connected  
392 to possible CO distribution variability.

### 393 **Acknowledgments**

394 We thank to the staff of the HHSMT for crucial support while observing, and  
395 to J.-L Bertaux and to F. Montmessin for providing us the SPICAV data par-  
396 allel to publication. We also thank the two manuscript referees for their crit-  
397 icism and valuable suggestions for improvement of the initial submission. We  
398 acknowledge JPL's Horizons online ephemeris generator for providing Venus's  
399 position during the observations. This research has made use of NASA's As-  
400 trophysics Data System.

### 401 **References**

402 Bertaux, J.-L., Vandaele, A.-C., Korablev, O., Villard, E., Fedorova, A.,  
403 Fussen, D., Quémerais, E., Belyaev, D., Mahieux, A., Montmessin, F.,  
404 Muller, C., Neefs, E., Nevejans, D., Wilquet, V., Dubois, J. P., Hauchecorne,  
405 A., Stepanov, A., Vinogradov, I., Rodin, A., Bertaux, J.-L., Nevejans, D.,  
406 Korablev, O., Montmessin, F., Vandaele, A.-C., Fedorova, A., Cabane, M.,  
407 Chassefière, E., Chaufray, J. Y., Dimarellis, E., Dubois, J. P., Hauchecorne,  
408 A., Leblanc, F., Lefèvre, F., Rannou, P., Quémerais, E., Villard, E., Fussen,  
409 D., Muller, C., Neefs, E., van Ransbeeck, E., Wilquet, V., Rodin, A.,

410 Stepanov, A., Vinogradov, I., Zasova, L., Forget, F., Lebonnois, S., Titov,  
411 D., Rafkin, S., Durry, G., Gérard, J. C., Sandel, B., Nov. 2007. A warm layer  
412 in Venus' cryosphere and high-altitude measurements of HF, HCl, H<sub>2</sub>O and  
413 HDO. *Nature* 450, 646–649.

414 Clancy, R. T., Muhleman, D. O., Jan. 1991. Long-term (1979-1990) changes  
415 in the thermal, dynamical, and compositional structure of the Venus meso-  
416 sphere as inferred from microwave spectral line observations of C-12O, C-  
417 13O, and CO-18. *Icarus* 89, 129–146.

418 Clancy, R. T., Sandor, B. J., Moriarty-Schieven, G. H., Jan. 2003. Observa-  
419 tional definition of the Venus mesopause: vertical structure, diurnal varia-  
420 tion, and temporal instability. *Icarus* 161, 1–16.

421 Clancy, R. T., Sandor, B. J., Moriarty-Schieven, G. H., Dec. 2005. Extreme  
422 Global Variability in the Middle Atmosphere of Venus. AGU Fall Meeting  
423 Abstracts, A223+.

424 Gruszka, M., Borysow, A., Sep. 1997. Roto-Translational Collision-Induced  
425 Absorption of CO<sub>2</sub> for the Atmosphere of Venus at Frequencies from 0 to  
426 250 cm<sup>-1</sup>, at Temperatures from 200 to 800 K. *Icarus* 129, 172–177.

427 Hartogh, P., Hartmann, G. K., 1990. A high-resolution chirp transform spec-  
428 trometer for microwave measurements. *Meas. Sci. Technol.* (1), 592–595.

429 Hartogh, P., Jarchow, C., 2004. The microwave brightness of planetary  
430 atmospheres—preparatory modeling for GREAT and HIFI. In: Amano, T.,  
431 Kasai, Y., Manabe, T. (Eds.), *Proceedings of the International Workshop  
432 on Critical Evaluation of mm-/submm-wave Spectroscopic Data for Atmo-  
433 spheric Observations, January 29-30, 2004, Ibaraki, Japan.* Communications  
434 Research Laboratory, pp. 75–78.

435 Jarchow, C., 1998. Bestimmung atmosphärischer Wasserdampf- und Ozon-  
436 profile mittels bodengebundener Millimeterwellen- Fernerkundung. Ph.D.

437 thesis.

438 Jarchow, C., Hartogh, P., 1995. Retrieval of data from ground-based mi-  
439 crowave sensing of the middle atmosphere: Comparison of two inversion  
440 techniques. In: Global Process Monitoring and Remote Sensing of Ocean  
441 and Sea Ice, EUROPTO-Series 2586. SPIE, Bellingham, pp. 196–205.

442 Kakar, R. K., Waters, J. W., Wilson, W. J., Jan. 1976. Venus - Microwave  
443 detection of carbon monoxide. *Science* 191, 379–+.

444 Kliore, A. J., Keating, G. M., Moroz, V. I., Apr. 1992. Venus international  
445 reference atmosphere (1985). *Planet. Space Sci.* 40, 573–573.

446 Lellouch, E., Goldstein, J. J., Rosenqvist, J., Bougher, S. W., Paubert, G.,  
447 Aug. 1994. Global circulation, thermal structure, and carbon monoxide dis-  
448 tribution in Venus’ mesosphere in 1991. *Icarus* 110, 315–339.

449 Rengel, M., Hartogh, P., Jarchow, C., 2008. HHSMT Observations of the  
450 Venusian Mesospheric Temperature, Winds, and CO abundance around the  
451 MESSENGER Flyby. *Advances in Geosciences* Accepted for publication.

452 Rodgers, C. D., Nov. 1976. Retrieval of Atmospheric Temperature and Com-  
453 position From Remote Measurements of Thermal Radiation. *Reviews of*  
454 *Geophysics and Space Physics* 14, 609–+.

455 Rodgers, C. D., Apr. 1990. Characterization and error analysis of profiles  
456 retrieved from remote sounding measurements. *J. Geophys. Res.* 95, 5587–  
457 5595.

458 Sandor, B. J., Clancy, R. T., Sep. 2005. Water vapor variations in the Venus  
459 mesosphere from microwave spectra. *Icarus* 177, 129–143.

460 Schofield, J. T., Taylor, F. W., Jan. 1983. Measurements of the mean, solar-  
461 fixed temperature and cloud structure of the middle atmosphere of Venus.  
462 *Quarterly Journal of the Royal Meteorological Society* 109, 57–80.

463 Seiff, A., Kirk, D. B., Jan. 1982. Structure of the Venus mesosphere and lower

464 thermosphere from measurements during entry of the Pioneer Venus probes.  
465 Icarus 49, 49–70.

466 Seiff, A., Kirk, D. B., Young, R. E., Blanchard, R. C., Findlay, J. T., Kelly,  
467 G. M., Sommer, S. C., Dec. 1980. Measurements of thermal structure and  
468 thermal contrasts in the atmosphere of Venus and related dynamical obser-  
469 vations - Results from the four Pioneer Venus probes. J. Geophys. Res. 85,  
470 7903–7933.

471 Villanueva, G., Hartogh, P., 2006. The high resolution chirp transform spec-  
472 trometer for the SOFIA-GREAT instrument. Experimental Astronomy 18,  
473 77–91.

474 Wilson, W. J., Klein, M. J., Kahar, R. K., Gulkis, S., Olsen, E. T., Ho, P. T. P.,  
475 Mar. 1981. Venus. I - Carbon monoxide distribution and molecular-line  
476 searches. Icarus 45, 624–637.

477 Table 1: Observation Parameters for the  $^{12}\text{CO}$  J = 2–1 line

478 Fig. 1: Schematic of the beam locations on the Venus disc (for a 24 " disc  
479 diameter) where  $^{12}\text{CO}$  J=2–1 and  $^{12}\text{CO}$  J=3–2 line integrations are obtained  
480 (left and right panels, respectively). Solid lines indicate the Venus'equator and  
481 central meridian. Dashed circles indicate the approximate FWHM beam di-  
482 ameter.

483 Fig. 2: Schematic representation of the Venus disc showing the distribution of  
484 the points where a pencil beam spectrum has been calculated. The rings show  
485 the grouping of the dots. Within a ring each dot has the same distance from  
486 the centre of the Venus disc. Limb area is not to scale with respect to the disc.  
487 Shade area represents the disc corresponding to the solid body.

488 Fig. 3: Dayside (left) and nightside (right) normalized atmospheric temper-  
489 ature weighting functions as provided by  $^{12}\text{CO}$  J = 2–1 line. Each function

490 corresponds to a particular frequency offset from line centre (from 0 to 500  
491 MHz offset).

492 Fig. 4: Dayside (left) and nightside (right) normalized CO mixing weighting  
493 functions as provided by  $^{12}\text{CO}$   $J = 2-1$  line. Each function corresponds to a  
494 particular frequency offset from line centre (from 0 to 500 MHz offset).

495 Fig. 5: Temperature (left) and CO mixing weighting functions (right) as pro-  
496 vided by  $^{13}\text{CO}$   $J = 2-1$  line. Each function corresponds to a particular fre-  
497 quency offset from line centre (from 0 to 500 MHz offset).

498 Fig. 6: Synthetic spectra solution for observations in Table 1 (left upper pan-  
499 els), difference between the observed and fitted spectra (left lower panels),  
500 retrieved temperature, CO distribution and wind derived from the spectrum.  
501 The dash lines show the initial profiles, and the horizontal lines the error bars.

502 Fig. 7: continued

503 Fig. 8: continued

504 Fig. 9: continued

505 Fig. 10: continued

506 Fig. 11: continued

507 Fig. 12: Temperature profile retrieval (from Obs. 36), solid line, compared to  
508 the profile from the stellar occultations with the SPICAV onboard Venus Ex-  
509 press (Bertaux et al., 2007), PV descent probes (Seiff et al., 1980), from the  
510 OIR sounding measurements (Schofield and Taylor, 1983), and from the PV  
511 night probe (Seiff and Kirk, 1982). The SPICAV measurements were taken at  
512 latitude  $39^\circ$  N for orbits 95, 96, and 98, and latitude  $4^\circ$  S for orbits 102-104.  
513 The Pioneer-Venus derived VIRA reference profile for latitudes  $<30$  are indi-  
514 cated by the squares. The anomalously warm temperatures returned by the  
515 Venera 10 probe in 1975 are shown as stars symbols. The absolute uncertainty  
516 for the temperatures derived here is  $\pm 15$  K.

517 Fig. 13: Observed and fitted spectrum of  $^{12}\text{CO}$   $J = 2-1$  (Obs. 27, top left panel),  
518 the residual (difference between observation and fit, bottom left panel), and  
519 the retrieved vertical temperature and CO profiles (top centre and right pan-  
520 els) and respective kernels (low centre and right panels). The double peak in  
521 the centre of the residuum (left lower panel) is related to a frequency shift of  
522 the fitted line relative to the observed one: effect of winds causing Doppler  
523 shifts in the centre of the observed spectrum.

524 Fig. 14: Dayside (left) and nightside (right) wind weighting functions as pro-  
525 vided by  $^{12}\text{CO}$   $J = 2-1$  lines.

526 Fig. 15: Retrieved wind velocity measurements for different beam positions on  
527 the Venus' disc for two observing days. Squares: 14 June, Triangles: 15 June.  
528 Retrieved velocity error bars are indicated. E: East, W: West.

529 Fig. 16: Error patterns belonging to the temperature, mixing ratio and wind  
530 parts (upper, middle, and lower panels).

531 Fig. 17: Error patterns for the Obs. 34.

532 Fig. 18: Dayside (left) and nightside (right) HHSMT temperature profiles on  
533 14 June and 15 June (Obs. 29 and 34 for dayside with thin solid and dot-short  
534 dash lines, and Obs. 22 and 33 for nightside with thick solid and dot-short  
535 dash lines, respectively). Measurements from SPICAV (Bertaux et al., 2007)  
536 for orbits 102–104 are shown with dot-short, short dash-long, and dot-long  
537 dash lines, respectively, and from the PV night probe (Seiff et al., 1980) with  
538 triangles.

Table 1

## Observation Parameters

Beam	$d\alpha^a$	$d\delta^a$	Obs. No.	Scan No.	Line	Date	Receiver/Sideband
Position			June 2007				
5	0	0	19	139-140	$^{12}\text{CO J} = 2-1$	14	2mm/1.3mm ALMA - LSB
9	14	-2	20	141-146	$^{12}\text{CO J} = 2-1$	14	2mm/1.3mm ALMA - LSB
10	-14	3	21	147-152	$^{12}\text{CO J} = 2-1$	14	2mm/1.3mm ALMA - LSB
9	14	-2	22	153-156	$^{12}\text{CO J} = 2-1$	14	2mm/1.3mm ALMA - LSB
5	0	0	23	164-165	$^{12}\text{CO J} = 2-1$	14	2mm/1.3mm ALMA - LSB
9	14	-2	24	166-167	$^{12}\text{CO J} = 2-1$	14	2mm/1.3mm ALMA - LSB
11	19	-2	25	168-173	$^{12}\text{CO J} = 2-1$	14	2mm/1.3mm ALMA - LSB
12	-14	-19	26	174-176	$^{12}\text{CO J} = 2-1$	14	2mm/1.3mm ALMA - LSB
11	19	-2	27	177-182	$^{12}\text{CO J} = 2-1$	14	2mm/1.3mm ALMA - LSB
13	-19	3	28	183-188	$^{12}\text{CO J} = 2-1$	14	2mm/1.3mm ALMA - LSB
10	-14	3	29	189-194	$^{12}\text{CO J} = 2-1$	14	2mm/1.3mm ALMA - LSB
5	0	0	30	195-196	$^{12}\text{CO J} = 2-1$	14	2mm/1.3mm ALMA - LSB
5	0	0	31	199-202	$^{13}\text{CO J} = 2-1$	14	2mm/1.3mm ALMA - LSB
5	0	0	32	208-217	$^{12}\text{CO J} = 2-1$	15	2mm/1.3mm ALMA - LSB
14	16	-2	33	218-227	$^{12}\text{CO J} = 2-1$	15	2mm/1.3mm ALMA - LSB
15	-16	+3	34	228-237	$^{12}\text{CO J} = 2-1$	15	2mm/1.3mm ALMA - LSB
5	0	0	35	244-293	$^{13}\text{CO J} = 2-1$	15	2mm/1.3mm ALMA - LSB
5	0	0	36	295-299	$^{12}\text{CO J} = 2-1$	15	2mm/1.3mm ALMA - LSB

<sup>a</sup>  $d\alpha$  and  $d\delta$ , right ascension and declination, are the astronomical coordinates of a point on the celestial sphere when using the equatorial coordinate system. The earlier coordinate is the celestial equivalent of terrestrial longitude, and the later one, to the latitude, projected onto the celestial sphere.

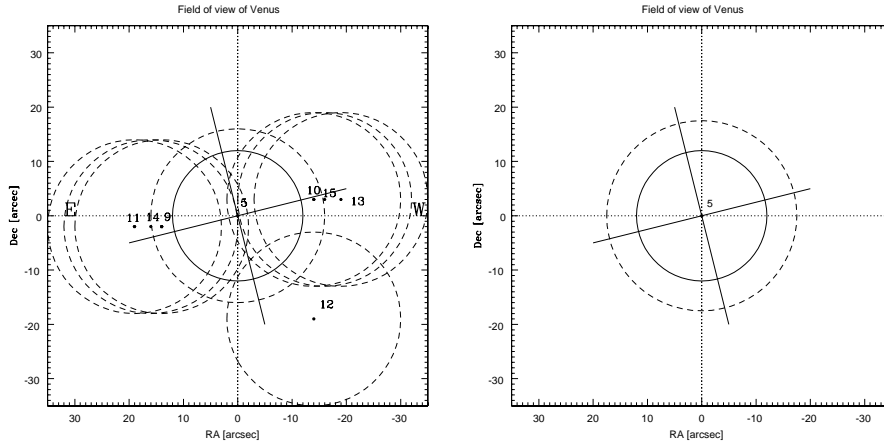


Fig. 1.

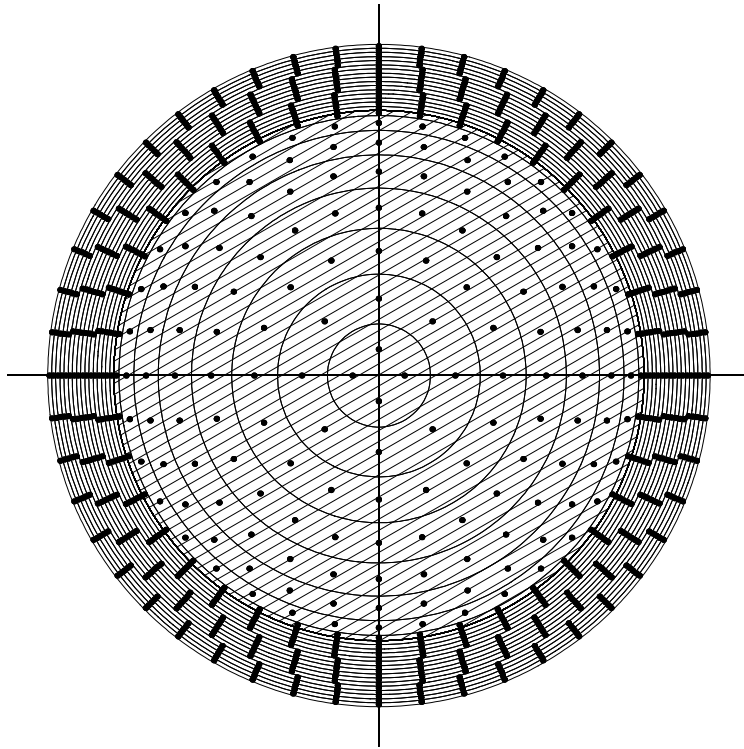


Fig. 2.

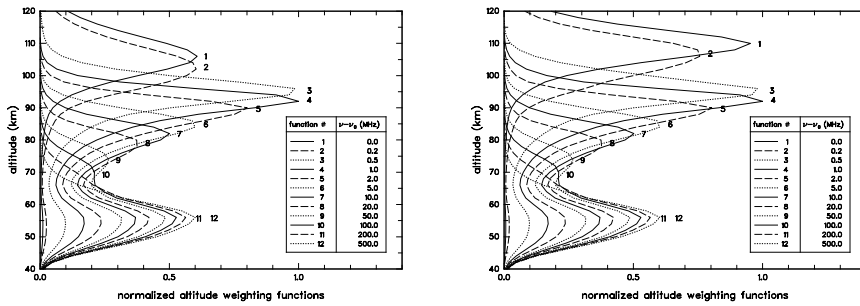


Fig. 3.

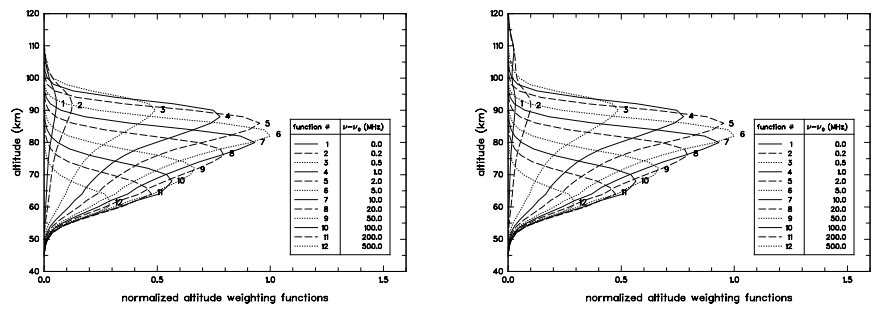


Fig. 4.

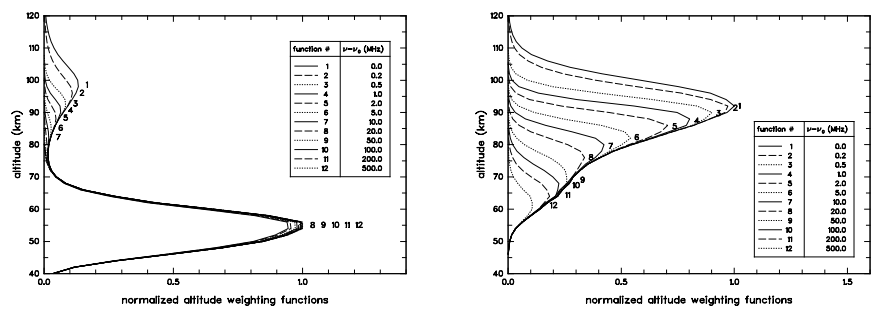


Fig. 5.

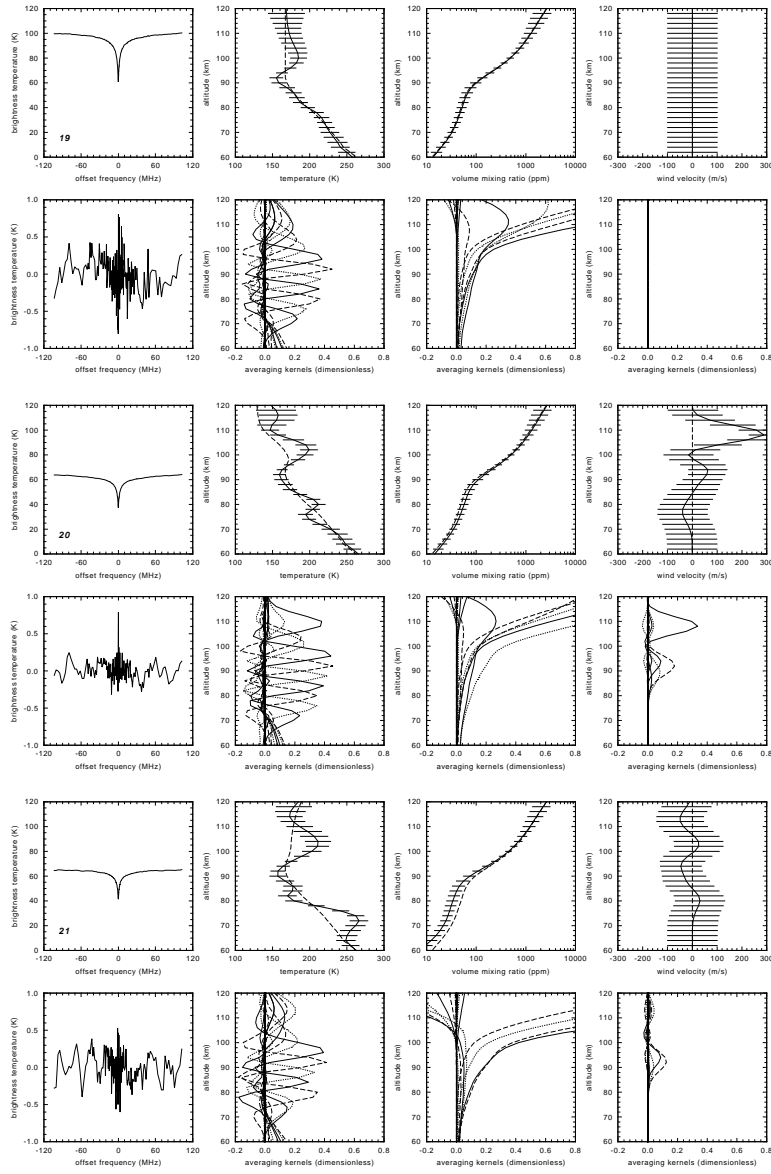


Fig. 6.

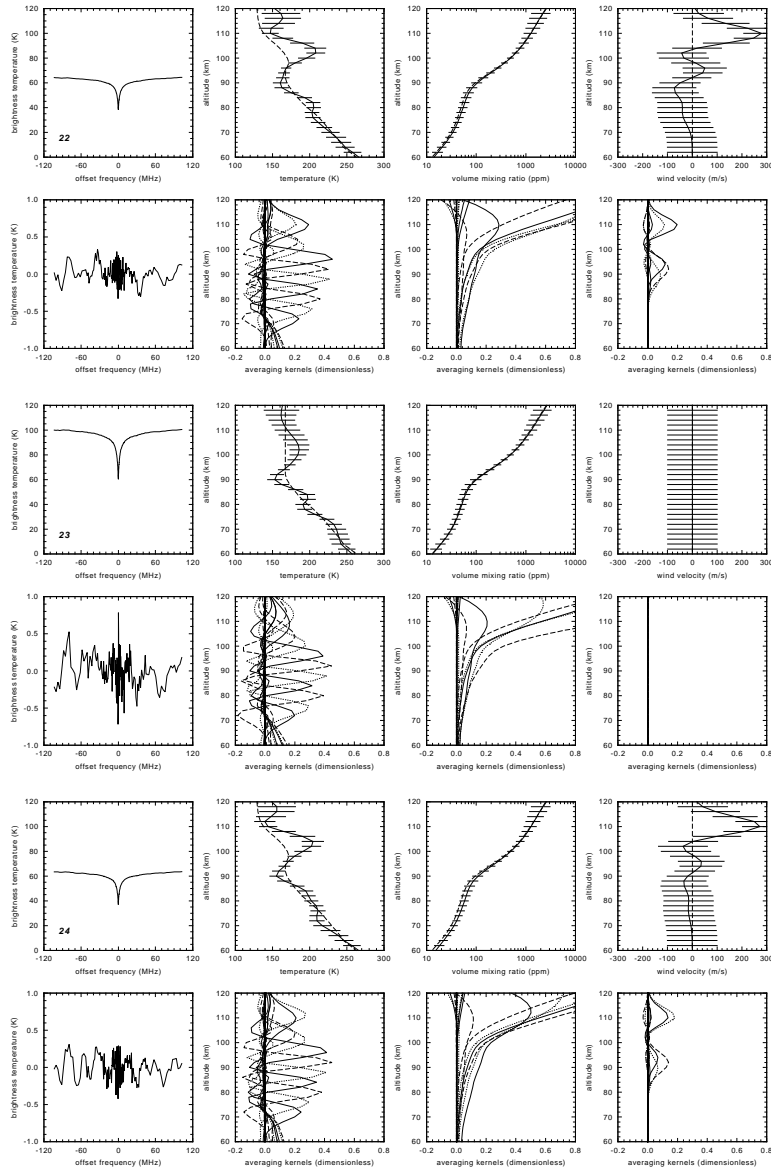


Fig. 7.

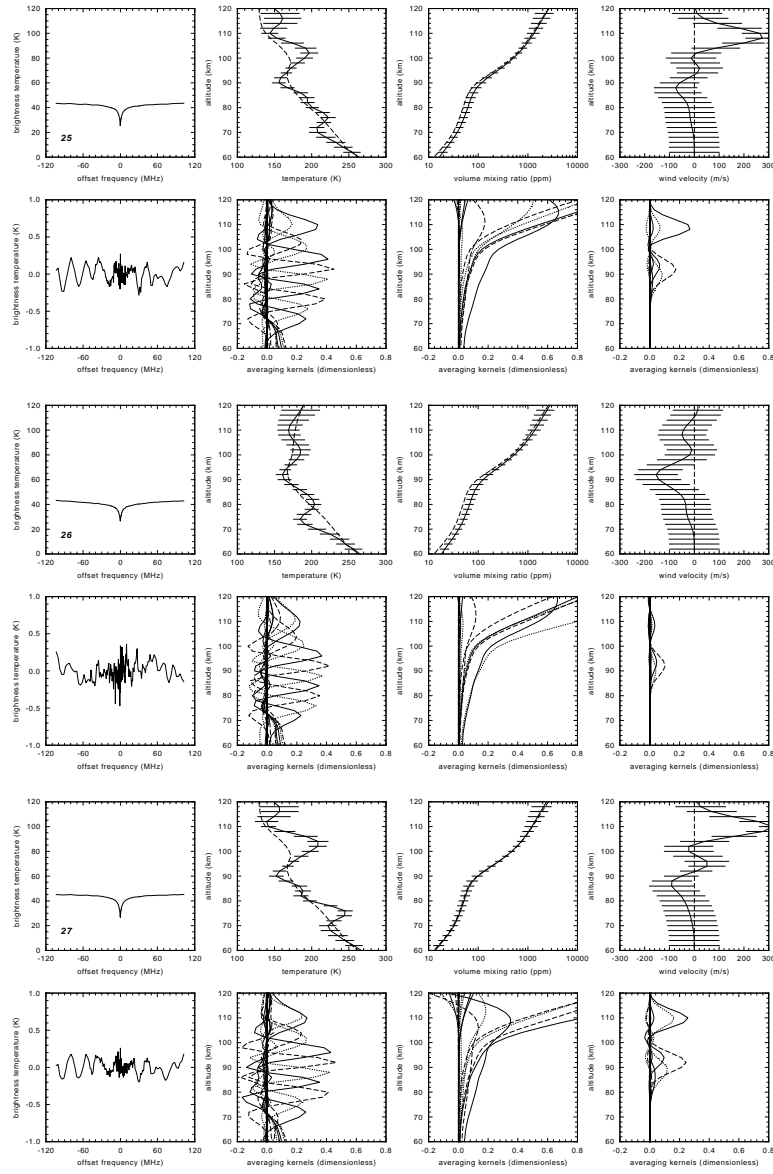


Fig. 8.

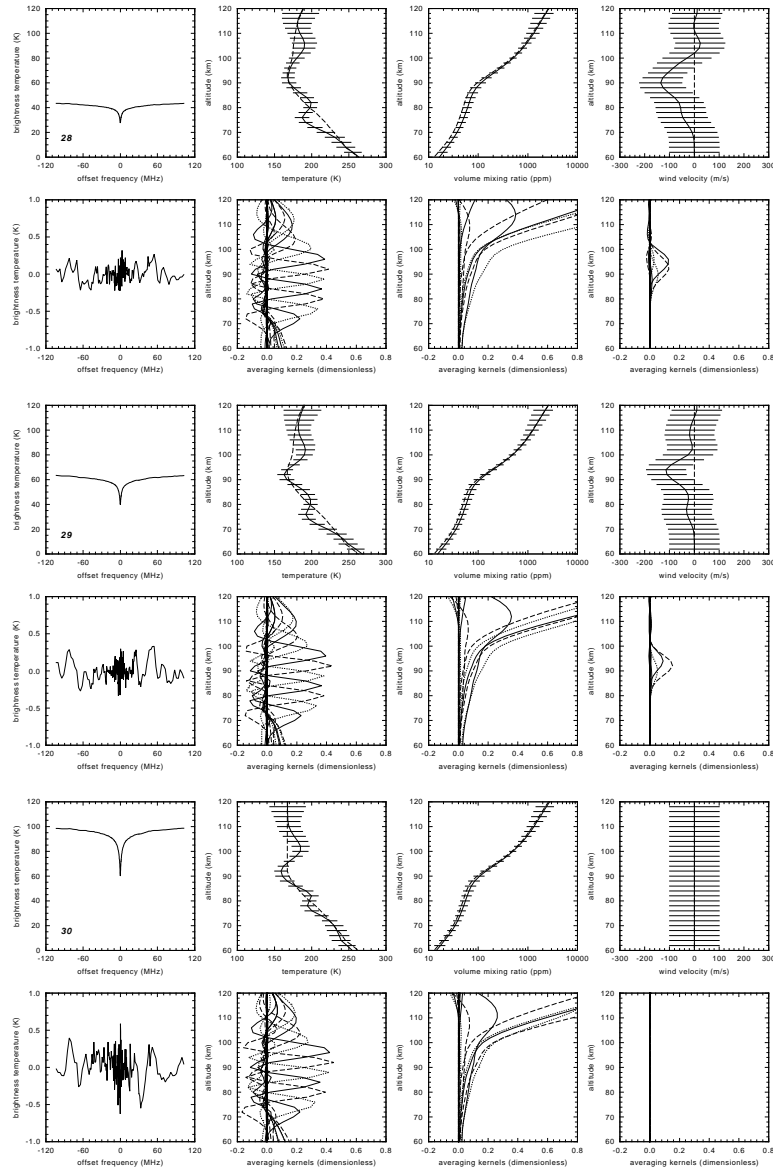


Fig. 9.

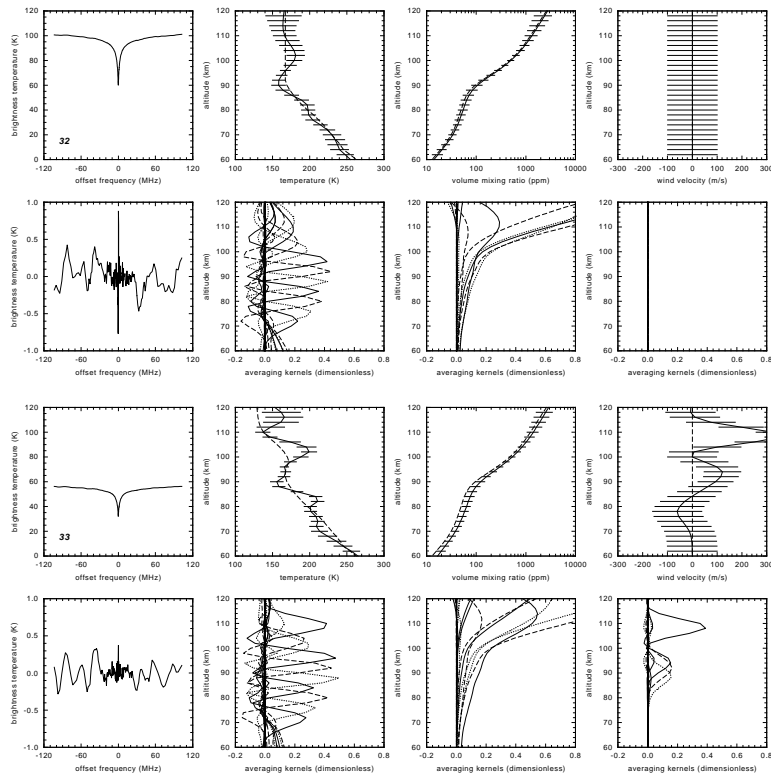


Fig. 10.

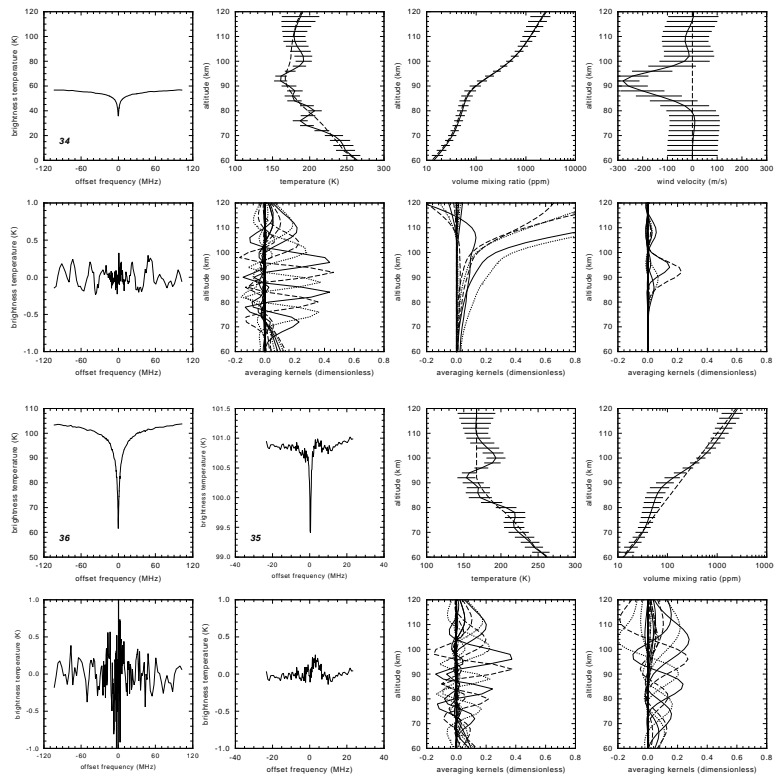


Fig. 11.

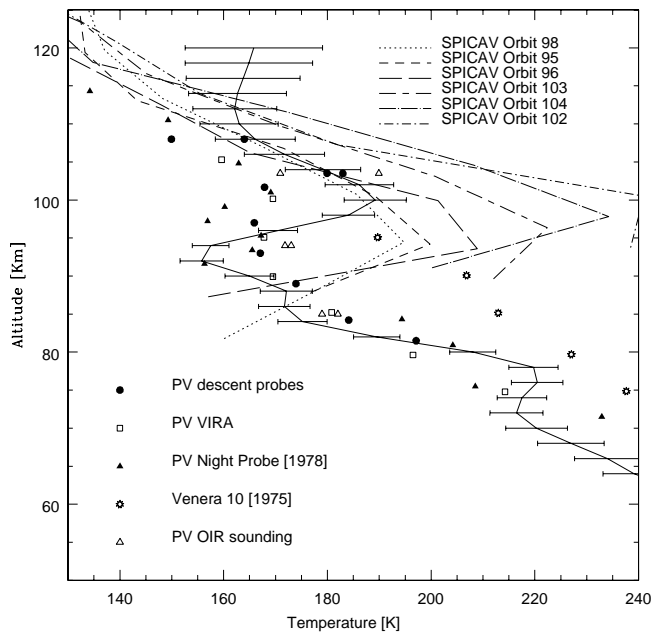


Fig. 12.

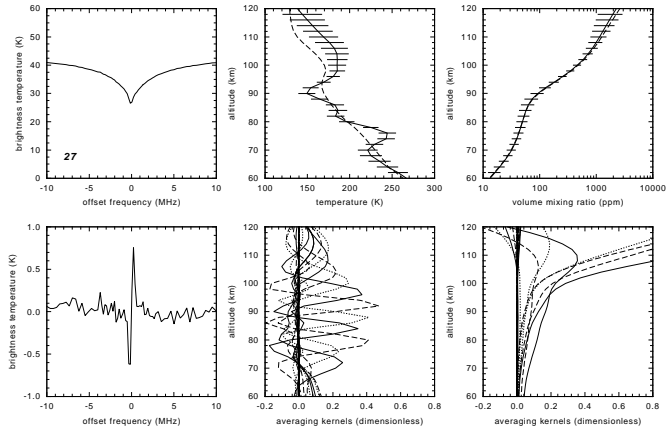


Fig. 13.

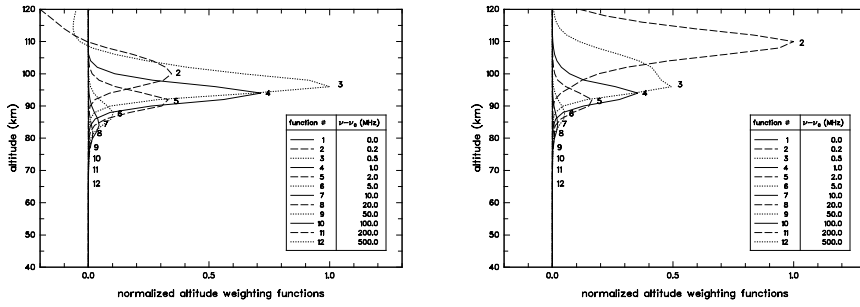


Fig. 14.

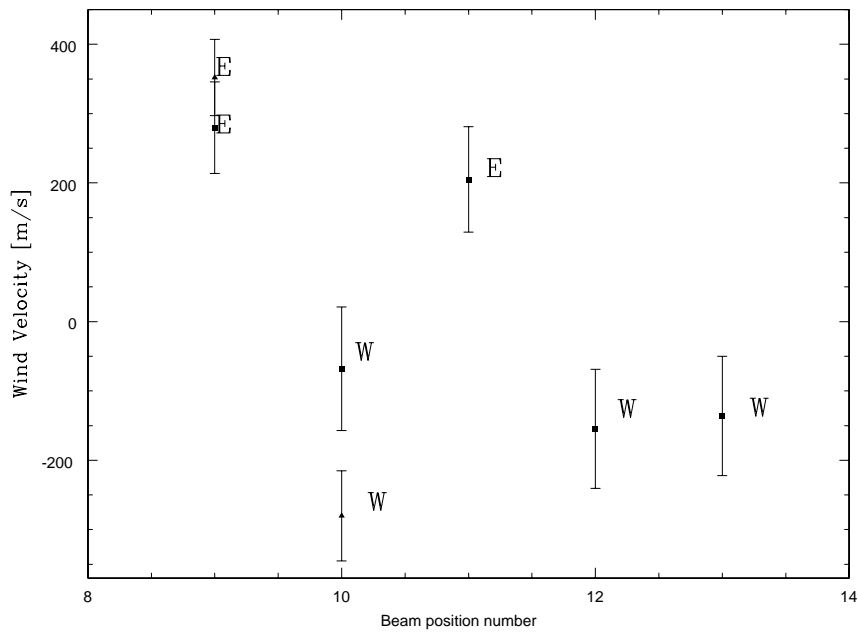


Fig. 15.

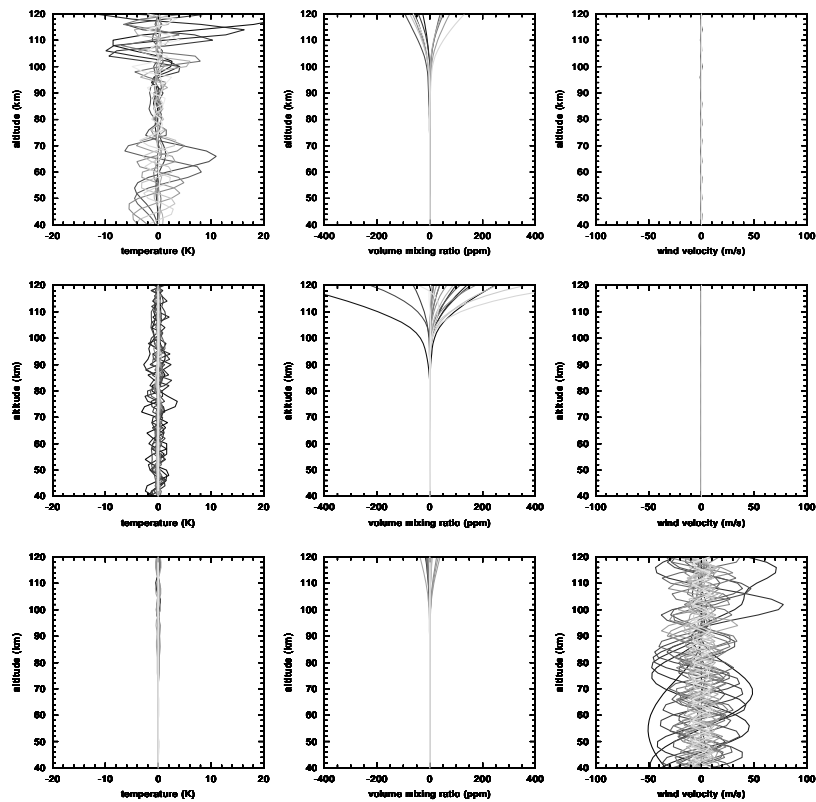


Fig. 16.

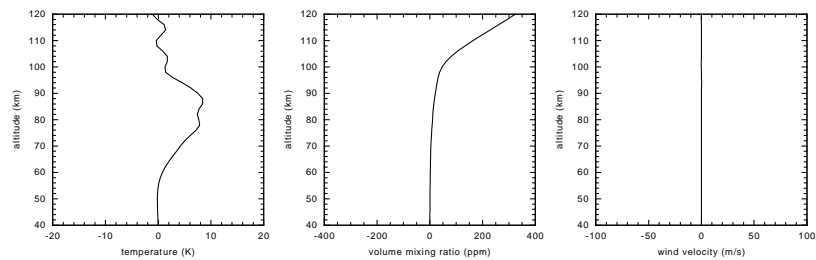


Fig. 17.

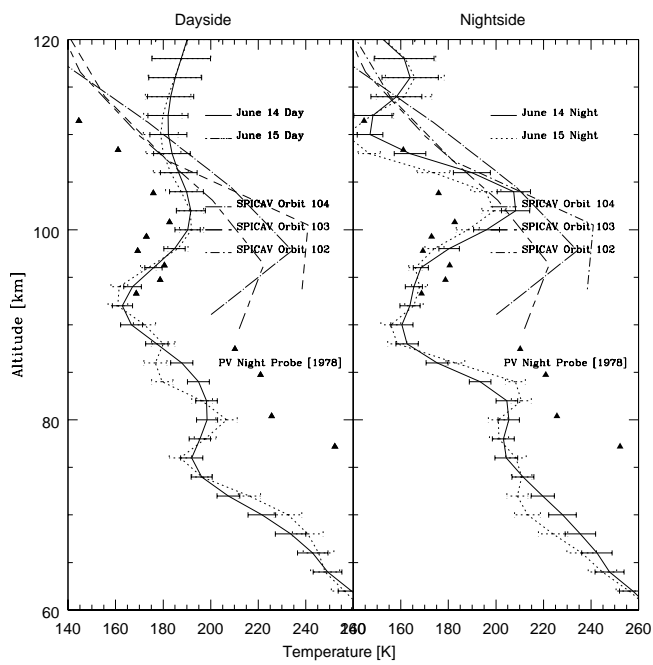


Fig. 18.